Temporal Frequency of Subthreshold Oscillations Scales with Entorhinal Grid Cell Field Spacing

Lisa M. Giocomo, *et al.*

Science **315**, 1719 (2007);
DOI: 10.1126/science.1139207

Science (print ISSN 0036-8075; online ISSN 1095-9203) is published weekly, except the last week in December, by the American Association for the Advancement of Science, 1200 New York Avenue NW, Washington, DC 20005.

however, the additional negative feedback allows exit from competence to occur at higher ComS and Rok concentrations, reducing the sensitivity of τ_{comp} to stochastic fluctuations (fig. S10).

It is not known whether competence initiation is controlled by noise, as in the model. To test the impact of noise on competence initiation, we set out to globally modulate the amount of noise in the cell. We used a *B. subtilis* strain in which the *ftsW* gene, which is necessary for septation, was replaced by an inducible copy. In the absence of inducer, septation was inhibited, resulting in elongated filamentous cells. Each filament was composed of multiple cell units, all sharing cytoplasm. Within a filament, diffusion is expected to effectively average cell contents, reducing noise in gene expression, without affecting mean concentrations of cellular components (Fig. 4A) (*17*). In some bacterial mutants that have elongated filamentous morphologies, cellular growth, nucleoid density, protein expression, and other physiological characteristics appear normal, even though cellular volume is greatly increased (fig. S12) (*18*–*20*). We integrated an inducible P_{hyp}-*yfp* construct and measured the effect of cell length on cell-cell fluctuations in yellow fluorescent protein (YFP) expression (Fig. 4B). We found that noise does indeed decrease with increasing length (Fig. 4B, inset). A simple model of transcription and translation (*21*–*24*) that incorporates the continuity of filamentous cell growth produced qualitatively similar results (Fig. 4B, inset, and SOM text). Thus, cell size can in this case be used to modulate gene expression noise.

How does noise affect the probability of initiation of competence? To answer this question, we induced filamentation in the conditional *ftsW* strain at the beginning of, or before, movie acquisition and quantified P_{init} as a function of cell length. We determined length distributions of cells at the moment they initiated competence, as detected by P_{comG} expression (Fig. 4C). As a comparison, we also measured length distributions for noncompetent cells at a similar distribution of times. We plotted the relative fraction of cells that initiated competence at a given length, compared with the total number of cells at that length. The results showed that P_{init} decreased as cells elongated (Fig. 4D and SOM text). A similar decrease in P_{init} was observed in corresponding simulations (Fig. 4D). To test if the reduction in P_{init} could be due to factors other than diminished noise, we examined two promoters, P_{comS} and P_{spo0A}, both strongly regulated under these conditions. Spo0A is a master regulator of sporulation, a competing starvation response, and high concentrations of Spo0A inhibit competence (*3*). Conversely, P_{comS} expression is necessary for competence. Mean expression of both P_{comS} and P_{spo0A} was unaffected by cell length (fig. S17). This supports the idea that gene expression levels are independent of cell length under these conditions and that P_{init} depends on noise.

Noise may play at least three different functional roles in competence. First, noise could be responsible for the observed variability in duration. Second, noise may be necessary to maintain excitability over a wide parameter range, by inducing escape from states of high ComK concentration. Third, noise appears to have a pivotal role in competence initiation (Fig. 4D) and thus should be considered alongside genetic parameters and circuit architecture to comprehensively understand differentiation at the single-cell level.

Quantitative analysis of a genetic system beyond its normal operating regime, including gene expression strengths, circuit architecture, and noise levels, strongly constrains dynamical models. The competence regulation system maintains excitable behavior over a broad range of parameter values. Experimentally, α_K and α_S enable P_{init} and τ_{comp} to be tuned independently, allowing the system, in theory, to adapt to independent selective pressures during evolution. The circuit can also access different dynamic regimes, such as oscillation and bistability, indicating its potential to evolve alternative qualitative behaviors.

References and Notes

1. U. Alon, *An Introduction to Systems Biology: Design Principles of Biological Circuits*. Mathematical and Computational Biology Series, vol. 10 (Chapman & Hall/CRC, Boca Raton, FL, 2006.
2. D. Dubnau, *Annu. Rev. Microbiol.* **53**, 217 (1999).
3. A. D. Grossman, *Annu. Rev. Genet.* **29**, 477 (1995).
4. G. M. Suel *et al.*, *Nature* **440**, 545 (2006).
5. R. M. Berka *et al.*, *Mol. Microbiol.* **43**, 1331 (2002).
6. D. van Sinderen *et al.*, *Mol. Microbiol.* **15**, 455 (1995).
7. H. Maamar, D. Dubnau, *Mol. Microbiol.* **56**, 615 (2005).
8. W. K. Smits *et al.*, *Mol. Microbiol.* **56**, 604 (2005).
9. K. Turgay *et al.*, *EMBO J.* **17**, 6730 (1998).
10. J. Hahn, L. Kong, D. Dubnau, *J. Bacteriol.* **176**, 5753 (1994).
11. M. Ogura *et al.*, *Mol. Microbiol.* **32**, 799 (1999).
12. C. Koch, *Biophysics of Computation* (Oxford Univ. Press, Oxford, 1999).
13. D. Dubnau, R. Losick, *Mol. Microbiol.* **61**, 564 (2006).
14. D. T. Gillespie, *J. Phys. Chem.* **81**, 2340 (1977).
15. The gene circuit shown in Fig. 1B can be described, in a continuous approximation, by two coupled differential equations that govern the dynamical evolution of the concentrations of ComK and ComS proteins, denoted K and S, respectively. The equation for K is $\frac{dK}{dt} = \alpha_k + \frac{\beta_k K^n}{k_k^n + K^n} - \frac{\delta_k K}{1 + K/\Gamma_k + S/\Gamma_s} - \lambda_k K$, where α_k and β_k parameterize the strength of constitutive and autoregulated ComK expression, respectively. The third term models degradation through competitive binding of ComK and ComS to MecA. The final term represents linear degradation of ComK. The equation for S is $\frac{dS}{dt} = \alpha_s + \frac{\beta_s}{1 + (K/k_s)^p} - \frac{\delta_s S}{1 + K/\Gamma_k + S/\Gamma_s} - \lambda_s S$. Here, α_s and β_s measure the strength of constitutive and regulated *comS* expression, respectively. The third and fourth terms represent MecA-mediated and linear degradation, respectively. Other parameters are defined in the SOM text. We have also developed a discrete model of the circuit that incorporates intrinsic noise explicitly. The requirement of independent tunability of P_{init} and τ_{comp} strongly constrains the allowed parameter values and thus the structure of the phase space. The modeling is described in detail in the SOM text.
16. T. T. Hoa *et al.*, *Mol. Microbiol.* **43**, 15 (2002).
17. M. B. Elowitz *et al.*, *J. Bacteriol.* **181**, 197 (1999).
18. F. Ishino *et al.*, *J. Bacteriol.* **171**, 5523 (1989).
19. N. Maki *et al.*, *J. Bacteriol.* **182**, 4337 (2000).
20. F. Tetart *et al.*, *Mol. Microbiol.* **6**, 621 (1992).
21. H. H. McAdams, A. Arkin, *Proc. Natl. Acad. Sci. U.S.A.* **94**, 814 (1997).
22. J. Paulsson, *Nature* **427**, 415 (2004).
23. P. S. Swain, M. B. Elowitz, E. D. Siggia, *Proc. Natl. Acad. Sci. U.S.A.* **99**, 12795 (2002).
24. M. Thattai, A. van Oudenaarden, *Proc. Natl. Acad. Sci. U.S.A.* **98**, 8614 (2001).

25. We thank R. Kishony, B. Shraiman, U. Alon, R. Ranganathan, S. Altschuler, L. Wu, and K. Süel, together with members of the Elowitz laboratory, for thoughtful comments and discussions. This work was supported by grants from NIH (R01 GM079771 to M.B.E. and GM068763 to the Center for Modular Biology), the Searle Scholars Program, the Human Frontiers Science Program, and the Packard Foundation. G.M.S. is supported by California Institute of Technology Center for Biological Circuit Design and the University of Texas Southwestern's Endowed Scholars Program. J.G.O. acknowledges financial support from the Ministerio de Educacion y Ciencia (Spain, project FIS2006-11452) and from the Generalitat de Catalunya.

Supporting Online Material

www.sciencemag.org/cgi/content/full/315/5819/1716/DC1
Materials and Methods
SOM Text
Figs. S1 to S17
Tables S1 to S4
References

13 November 2006; accepted 26 February 2007
10.1126/science.1137455

Temporal Frequency of Subthreshold Oscillations Scales with Entorhinal Grid Cell Field Spacing

Lisa M. Giocomo,[1]* Eric A. Zilli,[1] Erik Fransén,[2] Michael E. Hasselmo[1]*

Grid cells in layer II of rat entorhinal cortex fire to spatial locations in a repeating hexagonal grid, with smaller spacing between grid fields for neurons in more dorsal anatomical locations. Data from in vitro whole-cell patch recordings showed differences in frequency of subthreshold membrane potential oscillations in entorhinal neurons that correspond to different positions along the dorsal-to-ventral axis, supporting a model of physiological mechanisms for grid cell responses.

The entorhinal cortex plays an important role in encoding of spatial information (*1*–*3*) and episodic memory (*4*). Many layer II neurons of rat entorhinal cortex are grid cells, firing when the rat is in an array of spatial locations forming a hexagonal grid within the environment (*5*–*7*). The spacing of firing fields in the grid varies with anatomical position of the cell along the dorsal-ventral axis of entorhinal cortex, as measured by distance from the postrhinal border (*5*). Neurons closer to the dorsal border of entorhinal cortex have shorter distances between firing fields. Computa-

tional models explicitly predict that differences in grid field spacing should correspond to differences in intrinsic frequencies of neurons along the dorsal-to-ventral axis (*3*, *8*). This could provide systematic variation in the gain of a movement-speed signal for path integration (*2*, *3*, *9*).

Subthreshold membrane potential oscillations in entorhinal cortical stellate cells (*10*) arise from a single-cell mechanism involving voltage-sensitive currents (*11*–*13*) and could contribute to network dynamics (*14*). We recorded subthreshold oscillations from 57 stellate cells in layer II of medial entorhinal cortex (fig. S1) in slices from different anatomical positions along the dorsal-ventral axis by using whole-cell patch clamp techniques (*15*). The position of each horizontal slice was measured individually relative to the dorsal surface of the brain (Fig. 1A).

Stellate cells in dorsal entorhinal cortex showed higher temporal frequencies (f) of subthreshold membrane potential oscillations compared with lower frequencies in cells from more ventral entorhinal slices (Fig. 1B). Dorsal cells (n = 30) were defined as cells recorded in slices taken between 3.8 mm [the border with postrhinal cortex (*16*)] and 4.9 mm from the dorsal surface of the brain. Ventral cells (n = 27) were defined as cells recorded in slices between 4.9 and 7.1 mm from the dorsal surface. Because the group means of the frequency of subthreshold oscillations recorded from these populations (Fig. 1B) can depend upon the mean membrane potential voltage, we performed this analysis separately for data gathered at different approximate holding membrane potentials of –50 mV and –45 mV. The mean frequency in dorsal cells was significantly higher than the mean frequency in ventral cells for measurements at about –50 mV (dorsal mean $f \pm$ SEM = 6.42 ± 0.40 Hz and n = 28; ventral f = 4.23 ± 0.32 Hz and n = 25; $P < 0.001$) and –45 mV (dorsal mean $f \pm$ SEM = 7.18 ± 0.50 Hz and n = 14; ventral f = 4.88 ± 0.59 Hz and n = 7; $P < 0.01$). Frequencies were determined by an automated autocorrelation anal-

[1]Center for Memory and Brain, Department of Psychology, Program in Neuroscience, Boston University, 2 Cummington Street, Boston, MA 02215, USA. [2]School of Computer Science and Communication, Royal Institute of Technology and Stockholm Brain Institute, SE-100 44 Stockholm, Sweden.

*To whom correspondence should be addressed. E-mail: hasselmo@bu.edu (M.E.H.); giocomo@bu.edu (L.M.G.)

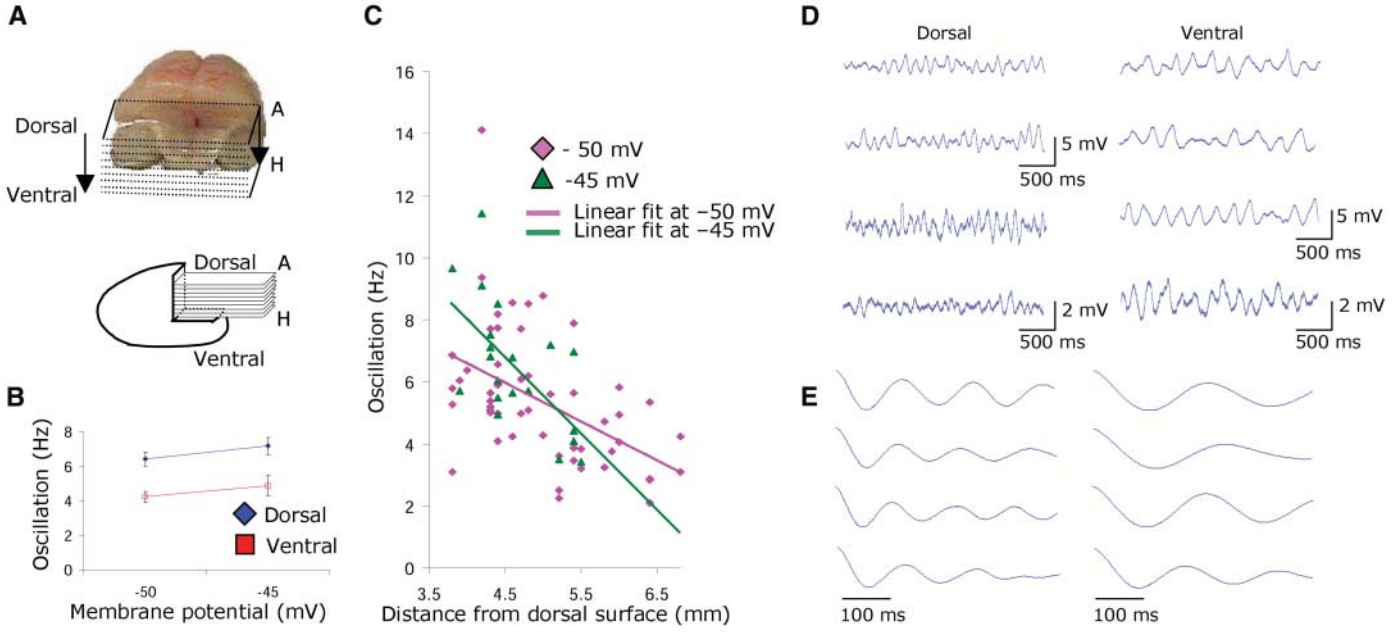

Fig. 1. Higher frequency of subthreshold oscillations in dorsal versus ventral entorhinal cortex. (**A**) Top, dorsal view of brain after slicing. Bottom, sagittal view showing anatomical location of horizontal slices A to H. (**B**) Mean frequency of subthreshold oscillations for neurons from dorsal slices (3.8 to 4.9 mm bregma) and ventral slices (4.9 to 7.1 mm bregma) at –50 mV and –45 mV. Error bars indicate SEM. (**C**) Subthreshold oscillation frequency plotted versus anatomical distance from dorsal surface. (**D**) Examples of subthreshold oscillations at –50 mV in dorsal regions (left) and ventral regions (right). (**E**) Corresponding autocorrelations used to measure frequency in (D).

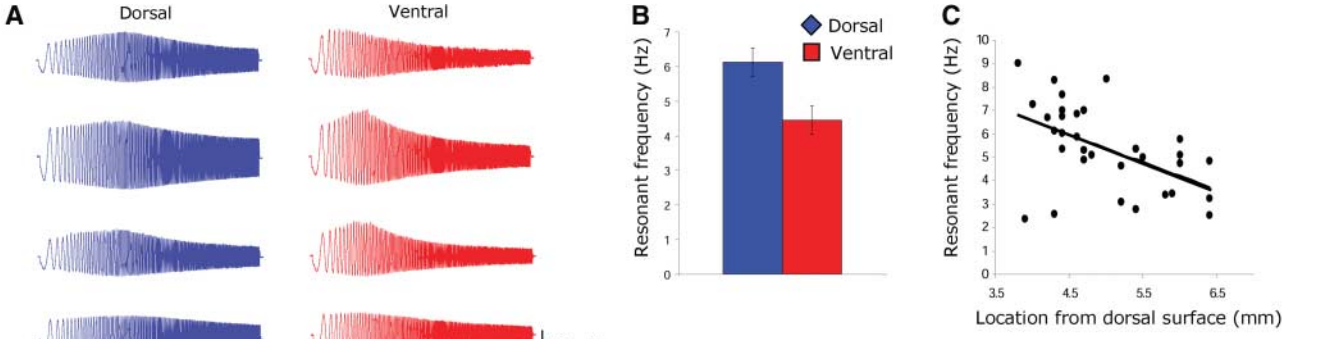

Fig. 2. Differences in resonance properties of neurons in dorsal versus ventral entorhinal cortex. (**A**) Examples of resonance responses of neurons in dorsal (blue) and ventral entorhinal cortex (red) in response to ZAP stimulus (black). (**B**) Histogram of mean peak resonance frequency for neurons in dorsal versus ventral entorhinal cortex. (**C**) Resonance frequency plotted versus anatomical distance from the dorsal surface.

ysis algorithm (*15*) and were used throughout unless otherwise noted. The significant difference between mean frequencies was replicated with analyses using the peak in the power spectra for data at –50 mV (dorsal $f = 4.86 \pm 0.37$ Hz and $n = 28$; ventral $f = 3.44 \pm 0.25$ Hz and $n = 25$; $P < 0.01$) and –45 mV (dorsal $f = 5.54 \pm 0.49$ Hz and $n = 14$; ventral $f = 3.76 \pm 0.31$ Hz and $n = 8$; $P < 0.01$) (fig. S2). The resting membrane potential, firing threshold, resistance, and age [dorsal mean age ± SEM = 19.8 ± 0.4 days and ventral age = 19.1 ± 0.4 days, P value not significant (NS)] did not contribute to the difference in the frequency of oscillations observed between neurons from dorsal versus ventral slices (*15*).

Entorhinal neurons showed a systematic difference in subthreshold oscillation frequency when plotted for different locations along the dorsal-ventral axis (Fig. 1C) for data at –50 mV ($r = 0.48$, slope = –1.26) and at –45 mV ($r = 0.60$, slope = –2.48). This pattern resembles the difference in spatial periodicity of grid cells previously recorded from layer II at different positions along the dorsal-ventral-axis in awake, behaving animals (*5*, *7*). Examples of subthreshold oscillations recorded from individual entorhinal neurons illustrate the difference in dorsal versus ventral frequency (Fig 1D). 500-ms segments of the autocorrelations computed for the same cells in Fig. 1D demonstrate the difference in peak-to-peak wavelength (Fig. 1E).

The frequency of subthreshold oscillations has been shown to correlate with the peak frequency of membrane potential resonance at rest (–60 to –64 mV) in entorhinal neurons (*17*). We evaluated the resonant frequency of neurons by delivering a 20-s-long impedance amplitude profile (ZAP) stimulus and measuring the input frequency that caused the largest amplitude depolarization of membrane potential. Individual examples of the response to the ZAP stimulus are shown for four neurons from dorsal entorhinal slices (Fig. 2A) and four neurons from more-ventral slices. The resonant frequency of stellate cells was significantly higher in dorsal cells compared with that in ventral cells (dorsal frequency = 6.13 ± 0.41 Hz and $n = 18$; ventral frequency = 4.45 ± 0.40 Hz and $n = 14$; $P < 0.01$) (Fig. 2B). There was no significant difference in resting potential between the populations used for this analysis (dorsal potential = –60.12 ± 0.26 mV and $n = 18$; ventral potential = –60.11 ± 0.26 mV and $n = 14$; P NS). Resonant frequency was systematically higher in dorsal regions when plotted in relation to anatomical location ($r = 0.51$, slope = –1.18) (Fig. 2C).

To analyze the relationship of subthreshold oscillations to other intrinsic properties, we measured the change in membrane potential during a hyperpolarizing current injection that usually caused a slow depolarizing shift (a "sag" of the membrane potential). The sag was fit with a dual exponential equation starting just after the trough of the sag and ending near the end of the current injection at steady state potential (Fig. 3, A and B). The faster of the two time constants (τ_1) of the sag was measured for hyperpolarizing current steps that ended at steady-state membrane voltages of –69.9 to –65 mV (V1) and at steady-state membrane voltages of –64.9 to –60 (V2). The time constant (τ_1) of the sag increased with depth on the dorsal-ventral axis (at V1, $r = 0.55$ and slope = 9.67; at V2, $r = 0.61$ and slope = 8.23) (Fig. 3C), with significantly faster values of τ_1 in more-dorsal portions compared with more-ventral portions at V1 (dorsal $\tau_1 = 23.37 \pm 1.24$ ms and $n = 17$; ventral $\tau_1 = 35.52 \pm 1.81$ ms, $n = 14$; $P < 0.01$) and at V2 (dorsal $\tau_1 = 22.37 \pm 1.60$ ms and $n = 11$; ventral $\tau_1 = 34.71 \pm 2.68$ ms and $n = 17$; $P < 0.01$). The τ_1 of the sag correlated with the frequency of subthreshold oscillations (at V1, $r = 0.63$ and slope = –4.32; at V2, $r = 0.65$ and slope = –4.10) (Fig. 3D). Voltage-clamp studies are necessary to confirm underlying currents. A potential candidate is the h current, which has been shown to underlie sag in stellate cells (*11*, *12*).

The differences in temporal frequency shown in this study correspond to differences in spatial periodicity of unit firing observed with extracellular recording in awake, behaving animals (*5*–*7*). Neurons at more-dorsal locations show higher intrinsic subthreshold oscillation frequency in vitro and smaller spacing between grid fields in vivo. Plots of the reciprocal of temporal frequency versus anatomical position (Fig. 4A) reveal slopes similar to the slope of grid field spacing (G) relative to anatomical position (Fig. 4B).

These data support the prediction of a model (SOM text) (*3*, *8*) related to other models of grid cells and theta phase precession (*18*–*20*). In this model, grid cell periodicity arises from an interference pattern generated by intrinsic temporal oscillations in the soma and dendrites of a single cell. During simulated rat movement, cells modulated by head direction and speed (*7*, *21*, *22*) shift the frequency of dendritic oscillations (consistent with voltage effects on frequency). The grid pattern is the product of interference by three

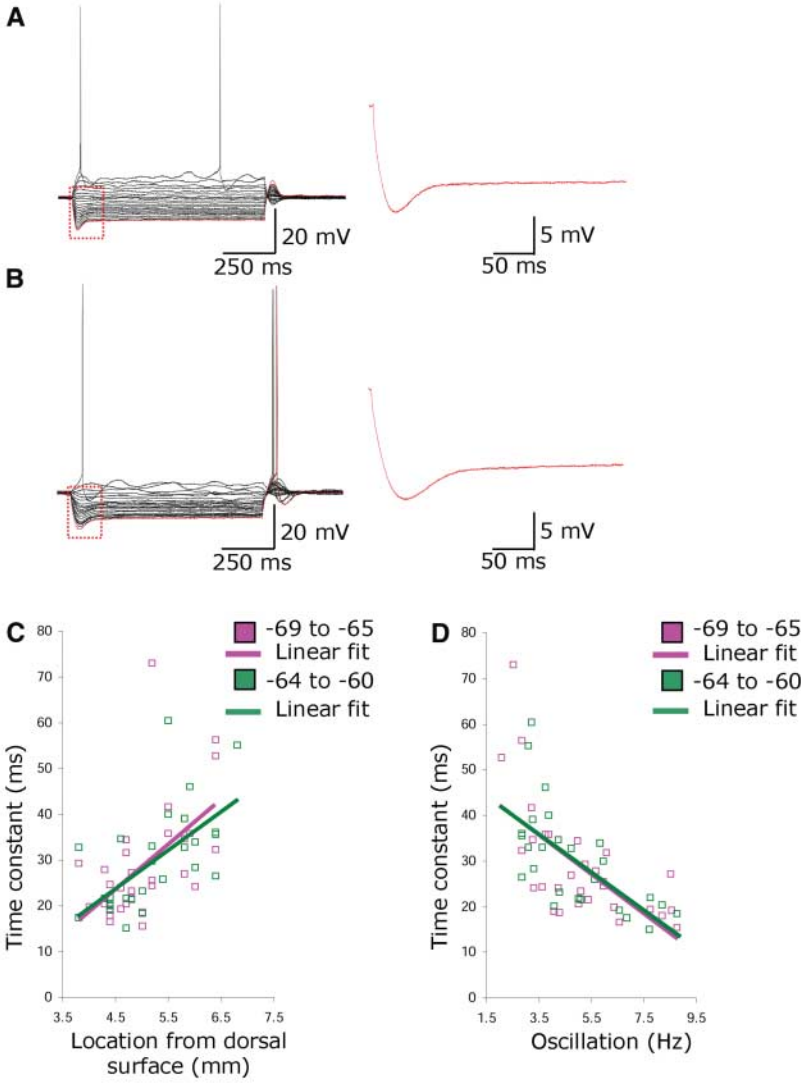

Fig. 3. Relationship of subthreshold membrane potential oscillations to sag potential. For single neurons in dorsal (**A**) and ventral entorhinal cortex (**B**), traces on left show membrane potential responses to multiple current injection levels. Single traces (right) show sag potentials at higher resolution. (**C**) τ_1 of sag potential (ms) plotted versus anatomical location. (**D**) τ_1 of sag potential plotted versus subthreshold oscillation frequency.

dendritic oscillations, each receiving a different head direction input, shifting in and out of phase with soma oscillations in proportion to distance moved in the preferred direction of each head direction cell. Spiking occurs when all three dendrites are in phase with the soma, causing oscillations to cross threshold (figs. S4 and S5). Spiking does not alter soma or dendritic phase but occurs with theta rhythmicity, consistent with in vivo recordings in entorhinal cortex (*5*–*7*) and hippocampus (*2*, *9*, *18*) and potentially causing precession relative to field potential oscillations (*3*, *8*, *19*, *20*).

The model (*3*, *8*) was modified to include shifts in dendritic frequency proportional to soma frequency and to use a scaling factor, $H = fG$ (fig. S6), determined from the experimental data. Simulations (SOM text) (Fig. 4, C and D) demonstrated that differences in temporal frequency of somatic oscillations result in different grid field spacing. Insertion of the experimentally determined value for subthreshold oscillation frequency (f) at a particular anatomical location resulted in simulated grid cell spacing that matches data (*7*) on grid cell spacing (G) at the same anatomical location (figs. S4 and S7).

The model demonstrates one possible mechanism for path integration (*2*) and supports the prediction that systematic variation in gain of a movement-speed signal could underlie differences in grid field spacing (*2*, *9*). The model is compatible with maintenance of grid cell representations by persistent firing (*23*) or attractor dynamics arising from patterned excitatory connectivity (*2*, *24*, *25*). Long-term stability of grid fields could require place cell input dependent on external landmarks (*3*, *8*, *26*). Differences in intrinsic frequency along the dorsal-ventral axis of entorhinal cortex could contribute to differences in place field size along the septal-to-temporal axis of the hippocampus (*9*, *27*).

The systematic differences in intrinsic temporal frequency may provide multiple scales for coding of both space and time. Periodic representation of the environment at multiple spatial scales could prove essential to mechanisms of path integration (*2*, *3*, *9*, *28*), consistent with impairments after entorhinal lesions (*1*). Coding of continuous dimensions by interacting frequencies could also allow the coding of continuous relative time necessary for episodic memory (*29*). These results suggest that, beyond simple summation of input, neural processing involves interactions of synaptic input and interference between intrinsic frequencies (*8*, *9*, *18*, *19*).

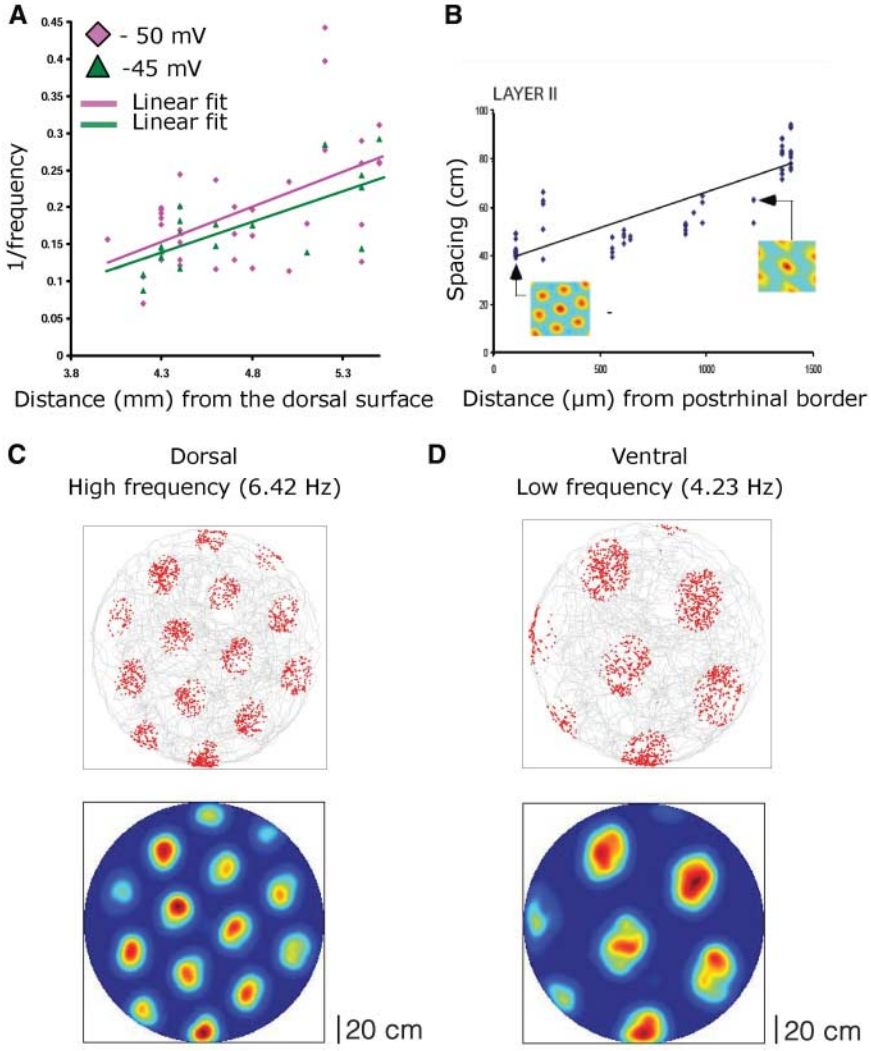

Fig. 4. Subthreshold oscillations may underlie differences in grid field spacing. (**A**) Reciprocal of oscillation frequency plotted versus anatomical depth for anatomical range matching a previous publication (*7*) as shown in (**B**). (**C** and **D**) Simulations of grid cell model (*3*, *8*). Top, gray indicates trajectory of simulated rat. Red indicates firing locations. Bottom, firing rate map (red, maximum; blue, no spikes). Grid field spacing is small for mean dorsal oscillation frequency of 6.42 Hz (C) and larger for mean ventral frequency of 4.23 Hz (D).

References and Notes

1. H. A. Steffenach, M. Witter, M.-B. Moser, E. I. Moser, *Neuron* **45**, 301 (2005).
2. B. L. McNaughton, F. P. Battaglia, O. Jensen, E. I. Moser, M.-B. Moser, *Nat. Rev. Neurosci.* **7**, 663 (2006).
3. J. O'Keefe, N. Burgess, *Hippocampus* **15**, 853 (2005).
4. H. Eichenbaum, N. J. Cohen, *From Conditioning to Conscious Recollection* (Oxford Univ. Press, New York, 2003).
5. T. Hafting, M. Fyhn, S. Molden, M.-B. Moser, E. I. Moser, *Nature* **436**, 801 (2005).
6. M. Fyhn, S. Molden, M. P. Witter, E. I. Moser, M.-B. Moser, *Science* **305**, 1258 (2004).
7. F. Sargolini *et al.*, *Science* **312**, 758 (2006).
8. N. Burgess, C. Barry, J. O'Keefe, *Hippocampus*, in press.
9. A. P. Maurer, S. R. VanRhoads, G. R. Sutherland, P. Lipa, B. L. McNaughton, *Hippocampus* **15**, 841 (2005).
10. A. Alonso, R. R. Llinas, *Nature* **342**, 175 (1989).
11. C. T. Dickson *et al.*, *J. Neurophysiol.* **83**, 2562 (2000).
12. E. Fransen, A. A. Alonso, C. T. Dickson, J. Magistretti, M. E. Hasselmo, *Hippocampus* **14**, 368 (2004).
13. J. A. White, R. Klink, A. Alonso, A. R. Kay, *J. Neurophysiol.* **80**, 262 (1998).
14. C. D. Acker, N. Kopell, J. A. White, *J. Comput. Neurosci.* **15**, 71 (2003).
15. Materials and methods are available on *Science* Online.
16. G. Paxinos, C. Watson, *The Rat Brain in Stereotaxic Coordinates* (Academic Press, San Diego, CA, 1998).
17. I. Erchova, G. Kreck, U. Heinemann, A. V. Herz, *J. Physiol.* **560**, 89 (2004).
18. J. O'Keefe, M. L. Recce, *Hippocampus* **3**, 317 (1993).
19. M. Lengyel, Z. Szatmary, P. Erdi, *Hippocampus* **13**, 700 (2003).
20. H. T. Blair, A. C. Welday, K. Zhang, *J. Neurosci.*, in press.
21. J. S. Taube, J. P. Bassett, *Cereb. Cortex* **13**, 1162 (2003).
22. P. E. Sharp, H. T. Blair, J. Cho, *Trends Neurosci.* **24**, 289 (2001).
23. E. Fransén, B. Tahvildari, A. V. Egorov, M. E. Hasselmo, A. A. Alonso, *Neuron* **49**, 735 (2006).
24. M. C. Fuhs, D. S. Touretzky, *J. Neurosci.* **26**, 4266 (2006).
25. A. Samsonovich, B. L. McNaughton, *J. Neurosci.* **17**, 5900 (1997).
26. J. J. Knierim, H. S. Kudrimoti, B. L. McNaughton, *J. Neurophysiol.* **80**, 425 (1998).
27. T. Solstad, E. I. Moser, G. T. Einevoll, *Hippocampus* **16**, 1026 (2006).
28. A. D. Redish, D. S. Touretzky, *Hippocampus* **7**, 15 (1997).
29. M. E. Hasselmo, H. Eichenbaum, *Neural Netw.* **18**, 1172 (2005).

30. Thanks to E. Moser, M.-B. Moser, M. Yoshida, K. Lillis, H. Eichenbaum, and J. White for advice and comments. Research supported by National Institute of Mental Health (NIMH) grant MH60013, Silvio O. Conte Center grant NIMH MH71702, NSF Science of Learning Center SBE 0354378, and National Institute on Drug Abuse grant DA16454 (part of the Collaborative Research in Computational Neuroscience program).

Supporting Online Material

www.sciencemag.org/cgi/content/full/315/5819/1719/DC1
Materials and Methods
SOM Text
Figs. S1 to S7

22 December 2006; accepted 23 February 2007
10.1126/science.1139207

Supporting Online Material for

Temporal Frequency of Subthreshold Oscillations Scales with Entorhinal Grid Cell Field Spacing

Lisa M. Giocomo*, Eric A. Zilli, Erik Fransén, Michael E. Hasselmo*

* To whom correspondence should be addressed.
E-mail addresses: giocomo@bu.com, hasselmo@bu.edu

This file includes:

Materials and Methods
Supplementary Text
Figs. S1-S7
Supplemental References

Total Size: 660 KB

Materials and Methods

General Materials and Methods

These supporting materials describe the experimental methods, the data analysis techniques, algorithms and quantitative analysis of the relationship between subthreshold temporal frequency and the spatial frequency of grid fields recorded from grid cells in awake behaving animals.

All experiments were performed using brain slices prepared from young (17 – 23 days old), male and female Long-Evans rats, which were deeply anesthetized with Isoflurane and rapidly decapitated. Techniques were reviewed and approved by the Institutional Animal Care and Use Committee at Boston University. The brain was removed under 4 ºC artificial cerebrospinal fluid (ACSF) oxygenated by bubbling 95% O_2 / 5% CO_2 through the solution (the concentrations of compounds in the ACSF in millimolar were: NaCl[126.0], KCl[3], $MgSO_4$[2], Dextrose[10.0], $NaHCO_3$[26.0], NaH_2PO_4[1.25], $CaCl_2$[2]).

All recordings were performed in horizontal slices of entorhinal cortex. To control for the duration of slicing for different depths within the brain, the brain was sliced in different directions for different experiments with the brain mounted on either its dorsal surface or ventral surface. 17% of dorsal cells came from preparations sliced in the ventral to dorsal direction, and 83% from the dorsal to ventral direction. There was not a significant difference between the mean dominant oscillation frequency for dorsal cells taken from either preparation ($p = .63$ for autocorrelations at −50 mV; $p = .40$ for power spectra at −50 mV). 44% of ventral cells came from preparations sliced in the ventral to dorsal direction, and 56% from the dorsal to ventral direction. There was not a significant difference between the mean dominant oscillation frequency for ventral cells taken from either preparation ($p = .36$ for autocorrelations at −50 mV; $p = .28$ for power spectra at −50 mV). Before slicing, but after being glued to the slice mount, the brain was cut into quarters through the corpus callosum, to separate the hemispheres, and at approximately 8 mm from the rostral end of the brain (-4 mm Bregma), to preserve the frontal portion of the brain and allow for later measurement of slice depth. Four hundred micron (400 μm) slices were then cut in oxygenated 2.5 ºC ACSF using a vibroslicer. The full set of horizontal slices was kept from different positions along the dorsal to ventral axis. Slices were placed in a holding chamber, which had been divided into 8 different sub-chambers. The first slices, from both the left and right hemisphere of the brain, were placed in chamber A. The two subsequent slices were placed in the next chamber, B, and so on until each of the 8 slices from each hemisphere at each depth had been placed in chambers A-H. For all dorsal to ventral slices (100%), after slices were taken, the depth of the last slice was measured at approximately 2 mm lateral from the midline and −4 mm Bregma, where the frontal portion of the brain had been cut away (at approximately 0 mm Bregma). The location of other slices was then determined from the depth of the last slice taken. For ventral to dorsal slices, slicing started at approximately 7 mm from the dorsal surface of the brain. Measurements of a subset of ventral to dorsal slices (35%) confirmed a consistent slicing depth for this slice orientation. The location of the slice

was defined as the middle of the 400 micron range the slice covered (e.g. 4.2 mm from the dorsal surface for a slice covering the range of 4.0 to 4.4 mm from the dorsal surface).

The slices were stored in room temperature ACSF for a minimum of 1 hour before they were transferred to a submerged recording chamber on a fixed stage with continuously flowing ACSF kept at the physiologically realistic temperature of 37.5 ± .5ºC. For all experiments, 2 mM kynurenic acid, a glutamatergic antagonist, and 100 μM picrotoxin, a $GABA_A$ receptor antagonist, were added to the bath perfusate to block excitatory and inhibitory synaptic transmission. Whole cell patch clamp recordings were made with patch pipettes pulled from 10 cm borosilicate glass capillary tubes. Patch pipettes were filled with an intracellular solution with the following concentrations (in mM) K-gluconate[120], HEPES[10], EGTA[0.2], KCl[20], MgCl[2], diTrisPhCr[7], Na_2ATP[4] and TrisGTP[0.3] (pH adjusted to 7.3 with KOH). The intracellular solution contained 0.1% biocytin for morphological identification and staining of the cells. When filled with the intracellular solution, the patch pipettes had a resistance of between 3 and 7 MΩ. Cells were visualized on an upright microscope mounted on a translation stage allowing movement in the x-y place and equipped with a 5x and 40x water-immersion objective lenses. Cells were viewed with a monochrome camera and 12-inch television screen. With this equipment, the location and laminar distribution of EC cells is easily discernible (*1, 2*).

Recordings were made from all cell types in layer II of medial entorhinal cortex, and the location of cells was confirmed morphologically for 77% of cells. Cell type was verified by electrophysiology (e.g. presence of sag or oscillations) and for most cells (30 out of 57) by later morphology. The morphologically unidentified cells had similar electrophysiological profiles to the identified stellate cells. 36 cells were identified as non-stellate pyramidal-like cells and 3 cells were identified as horizontal cells; these cells were not included in the current study. Tight seals (>1 GΩ) between the recording pipette and cell membrane were formed and ruptured with negative pressure. Current clamp recordings were amplified by a Multiclamp 700B. Signals were filtered at 10 kHz and digitized at a sampling frequency of 20 kHz (50 μs). Signals were then acquired into a Pentium based computer using Clampex 9.0 software. Following the completion of an experiment, slices were fixed in 4% paraformaldehyde solution and later processed to reveal intracellular biocytin as has been described below.

Recordings were analyzed from a total of 57 stellate cells, 30 of these cells came from dorsal portions of entorhinal cortex (defined as 3.8 mm Bregma to 4.9 mm Bregma), and 27 of these cells came from ventral portions of entorhinal cortex (defined as 4.9 mm Bregma to 7.1 mm Bregma). These definitions are based on the coordinates in Paxinos and Watson (*3*). All cells used were held for ≥ 15 minutes, had an input resistance of ≥ 35 MΩ, an action potential height of ≥ 50 mV from threshold to peak, and a resting potential of ≤ −50 mV. The liquid junction potential was not compensated for. Cells whose firing threshold occurred at < −53 mV were not included (n = 3) in the analysis.

Selection of stellate cells

This study focused on recordings from stellate cells, as these neurons show subthreshold

membrane potential oscillations in entorhinal cortex. The morphology of cells was observed using staining after biocytin injection during the experiment (Fig. S1). Histochemical processing was performed using a method similar to previously described techniques (*4, 5*). Tissue slices fixed in 4% paraformaldehyde were individually removed and washed (3 x 5 min) in 0.1 M Sodium phosphate buffer (NaPB), and then processed without additional sectioning. Next, a 30 minute incubation in PHT (0.1 M NaPB, 0.2% gelatin, 0.25% Triton X-100) was used to block the nonspecific binding sites. The slices were then labeled with an avidin-biotin-horseradish-peroxidase complex and left over night in PHT. The next day, slices were washed in PHT. First in brief washes (5 x 3 min) and then in a series of longer washes (6 x 1 hour) with the last wash continuing overnight. On the third day, slices were first washed 3 x 10 min in 0.1 M Tris-buffered saline (pH adjusted to 7.6 with HCl). Slices were then individually transferred to a 3,3'-diaminobenzidine solution (DAB substrate solution). The DAB reaction was stopped when the desired staining was reached by washing the slices in Tris-buffered saline (3 X 10 min). The slices were mounted on gelatinized glass slides, left to air dry for 5 minutes and then cover slipped using movial. The slides were allowed to dry in the dark for at least 24 hours, after which the slices were imaged using a microscope and Image-Pro Plus software on a PC running Windows.

Morphological characterization

Morphological determination of stellate versus pyramidal cell was based on previous characterization of stellate and non-stellate cells in layer II of entorhinal cortex (*6*). Stellate cells had multiple, thick primary dendrites. In some cases, the staining revealed dendrites extending profusely into layer I and the axon projecting down into deeper layers of entorhinal cortex. Pyramidal cells had a single primary dendrite extending from the cell body, often branching at the border between layer I and II before extending into layer I of entorhinal cortex. The pyramidal-like cells were often located in the deeper portions of layer II. Horizontal cells (n = 3) had a horizontally oriented cell body and two thick, primary dendrites that came from the cell body and extended out horizontally along the border between layer I and layer II of entorhinal cortex. Morphology was used to identify the cells in conjunction with the cell's electrophysiological profile (*7*). Current injection was used to bring the cell near firing threshold and determine the presence or absence of sinusoidal subthreshold oscillations. Stellate cells also showed, in most cases, a large and prominent sag current in response to a hyperpolarizing current injection.

Data analysis

Clampfit 9.0, MATLAB and Excel were used for data analysis. The resistance of the cell was calculated using the Multiclamp commander at the beginning of each experiment. To determine the dominant frequency of stellate cells, current injection was applied at a variety of levels (from 10 to 500 pA). Recordings were made continuously and current injections increased until the cell was near or at firing threshold. The analysis of frequency of subthreshold oscillations used segments of membrane potential recorded near firing threshold. The mean length of membrane potential recordings from each cell used for analysis was 40.7 ± 4.17 seconds, with a maximum of 100 seconds and a minimum duration for any cell of ten seconds. There was not a significant difference between the lengths of membrane potential recording used for dorsal cells versus ventral

cells (at −50 mV p = .17 ; at −45 mV p = .33). The analysis of subthreshold oscillation frequency utilized an automated procedure implemented using the MATLAB simulation package. The membrane potential recordings were divided into a number of windows of 3 seconds length that overlapped by 1.5 seconds. Any window containing a spike (determined by the presence of any sample in the recorded data having a membrane potential above 0 mV) was not considered for analysis. This allowed the measurement for frequency to only be conducted on pieces of data that were free of spikes for at least 3 seconds.

Autocorrelation Analysis

Autocorrelations on each window were performed to estimate the oscillation frequencies. Each short window of data was zero centered and the autocorrelation was calculated using the unbiased option in MATLAB's xcorr function. The frequency was determined as the inverse of the interval from the central peak to the first side peak. The frequencies of the three windows with the highest difference between the amplitudes of the side peak and the trough between the two peaks were averaged and recorded as the results for the cell. In all cases the autocorrelation measurements were double-checked to ensure that the measurement of the first side peak was correct and, in some cases, the measurement was corrected after the automated process.

Power Spectra Analysis

A separate data analysis computed frequency using the power spectra from a Fourier transform. A Hanning window was applied to each section of data and the fast Fourier transform was calculated. The peak frequency between 2 and 15 Hz, as well as the power at that frequency, were recorded for each short window and the peak frequencies of the three windows with the highest peak power were averaged and recorded as the frequency of the cell's subthreshold oscillation.

Resonant Frequency Analysis

To estimate the resonant frequency of the recorded cells, we used the impedance amplitude profile (ZAP) protocol, in which each cell was injected with a sinusoidal current that increased linearly from 0 to 20 Hz over the course of 20 seconds, generated by the chirp function in MATLAB. The power spectrum of the membrane voltage in response to the injection was divided by the power spectrum of the injected current to produce a function of input frequency versus impedance. The input frequency corresponding to the highest impedance was recorded as the cell's resonant frequency. The average of 10 trials was used to determine the average resonance frequency. The amplitude of the input was adjusted so that there was no more than a 10mV change in the membrane potential between the starting and ending points of the ZAP. If a cell's resting potential was higher or lower than −60 mV ± 5 mV, a steady current injection was used to bring the cell to −60 mV.

Statistics

The difference between means for dorsal versus ventral cells were analyzed with a two-tailed Student's t-test and p-values are reported. Regression lines were constructed using the least-squares method and r-values are reported.

Sag Analysis

The time course for the sag potential was analyzed in cells by characterizing the response to hyperpolarizing step current injections, which usually induced an initial strong hyperpolarization that decayed to a smaller hyperpolarized steady state potential. The strong hyperpolarization followed by the decay is referred to as a "sag" potential (*7, 8*). Sag was analyzed for a subset of stellate cells that showed a prominent sag and remained stable during the current step protocol for sag analysis (n = 40). Cells were not included for this time constant analysis if the size of the sag trough was less than 115% of the size of the steady state endpoint of the response to hyperpolarization (n = 6), if the baseline starting potential was less than −50 mV or more than −70 mV (n = 5), if the cell did not oscillate at –50 mV (n = 3), or if the cell did not have a stable trace (according to the criteria below) with an endpoint between −70.0 mV and −60.0 mV (n = 3). MATLAB was used to analyze the time constant of the sag. Current clamp data was fitted with a double exponential function:

$$(1) \qquad F = A1^{(-t/\tau_1)} + A2^{(-t/\tau_2)}$$

Current clamp traces were recorded following 1 second long negative injections of variable amplitude. Analysis was performed only on traces with an end point voltage of between –70.0 mV and - 60.0 mV. Sag potentials were used for the fitting, starting from the trough of the sag response (+7 ms, to pass the trough) and ending at end of the current pulse (–4 ms, to avoid any stimulation artifact). Time constants (τ_1) were used in the subsequent analysis. MATLAB 7.3 and the "NonlinearLeastSquares" method were used in conjunction with the function "exp2". Traces from cases where large perturbations, noise, or oscillations were seen were excluded. Traces where the curve was not monotonic in general, but had a clear inverted U-shape and traces whose ratio of A1/A2 was larger than 15 were also excluded. For the scatterplots shown in Fig. 3, the τ_1 for each cell was used from the trace whose endpoint was closest to –70.0 mV (V1) and the τ_1 from the trace whose endpoint was closest to –65.0 mV (V2), that had not been excluded due to any of the above reasons.

Supporting Text

Scaling factor H derived entirely from experimental data.

The experimental data presented in Fig. 4 shows a clear systematic relationship between the frequency of single cell subthreshold oscillations (*f*) recorded intracellularly and the grid cell spacing (*G*) measured for neurons in awake, behaving animals (*9-11*). The data in Fig. 4A shows our single cell subthreshold oscillation frequency data plotted as *1/f* versus position *z*. This has a very similar slope to data in Fig. 4B comparing grid field spacing (*G*) plotted versus position (*11*). Based on the regression lines in Fig. 4, at z = 4.1 cm, the membrane potential oscillation frequency of 7.38 Hz corresponds to grid spacing of 40 cm, and at z = 5.4 cm an oscillation frequency of 3.87 Hz corresponds to the grid spacing of about 80 cm. Thus, the data show a reciprocal relationship of $H/f = G$, where H is a scaling factor relating the two measurements. As shown in Fig. S6, we computed the constant H to quantify the scaling shown in main text Fig. 4 between the

single cell data (f) and the corresponding grid field spacing (G). At individual depths z, simple multiplication of the values of oscillation data for f (Hz) and grid spacing data for G (cm) give a scaling factor of approximately 300 (Hz-cm) (see Fig. S6 and Table). This value H describes the relationship:

$$(2) \qquad fG = H$$

Where f is the frequency of subthreshold membrane potential oscillations (mpo), G is the spacing between grid fields measured in the data (*11*), and H is the scaling factor of 300 Hz-cm where the units are (cycles(mpo)/sec)cm. H is determined entirely by matching our data with data from (*11*). The variation in the scaling factor in Fig. S6 may be due to noise or inaccuracies in the estimate of f and G based on linear regression, or may reflect a small term dependent on the negative reciprocal of z.

This value can be used to relate the observed value of grid cell spacing (G) at a particular anatomical position along the dorsal-ventral axis to the value of the intrinsic subthreshold oscillation frequency (f) observed at that same anatomical position. This relationship can be computed by dividing H = 300 (Hz-cm) by G (in cm) to generate the value f (in Hz). For example, at 4.1 mm from the dorsal surface, the estimated mean value of G = 40 cm corresponds to an intrinsic frequency of $H/G = f$ = 7.5 Hz in our in vitro data, and at 5.4 mm from the dorsal surface, the estimated value of G = 80 cm corresponds to $H/G = f$ = 3.75 Hz in our data on subthreshold oscillations. This experimentally determined scaling factor proves essential to scaling in the simulation of grid cells presented in the next section.

Modeling of spatial periodicity based on temporal frequency.

The model proposed in (*12-14*) presents a mechanism showing how the frequency of subthreshold membrane potential oscillations could underlie grid cell field spacing, as simulated in Fig. 4 and Figs. S4-S5. Here we show how this model specifically requires computation of the value of $H = fG$ in order to correctly simulate the grid cell spacing at anatomical position z due to the subthreshold oscillation frequency f at anatomical position z. This model extends previous models of theta phase precession in which oscillations of different frequencies result in a phase shift of peak depolarization relative to a carrier theta frequency (*14-17*).

In the Burgess and O'Keefe model, the pattern of grid fields generated by a single entorhinal cell results from interference patterns between the baseline subthreshold oscillation frequency of the neuron at the soma and separate subthreshold oscillations induced by synaptic input from head direction cells to different dendritic compartments connected with the soma. The recordings presented here correspond to the measurement of baseline frequency at the soma, but the demonstration of changes in frequency with changes in voltage shown here and previously (*7*) demonstrate how synaptic input to different dendritic compartments can separately shift the frequency of subthreshold oscillations. The morphology of stellate cells with multiple dendritic branches from the soma (see Fig. S1) may be ideal for the interaction of independent dendritic inputs. Note that this model of interactions of subthreshold membrane potential oscillations within

single neurons differs from the use of interactions between suprathreshold oscillations in a network model of grid cells with many similar mathematical properties (*18*).

The simulations shown in Fig. 4 and Fig. S4-S5 demonstrate how different baseline frequencies of subthreshold oscillations give different grid field spacing, with high subthreshold oscillation frequencies resulting in smaller distances between grid fields, and lower subthreshold oscillation frequencies resulting in larger distances between grid fields. This simulation used the Burgess and O'Keefe model with the following equation for subthreshold oscillations at the soma:

$$v_s = \cos(f 2\pi t) \quad (3)$$

Where f is the baseline frequency of subthreshold oscillations. The pattern of interference in the model arises from shifts in subthreshold oscillations in three different dendritic compartments due to synaptic input from at least three head direction cells that are dependent upon the current heading of the rat. For each dendrite d, these cause the following changes in frequency:

$$v_d = \cos((f + Bs\cos(\phi - \phi_{HD}))2\pi t) \quad (4)$$

Where f is the baseline frequency, s is the speed of the rat, ϕ is the direction of the rat, and ϕ_{HD} is the preferred direction for each of three different head direction cells. These oscillations are summed and the interaction from different dendrites is multiplied, after which a firing threshold is applied (in step function Θ) to obtain the resulting pattern of grid cell responses g.

$$g = \Theta[\prod_k (\cos(f 2\pi t) + \cos((f + Bs\cos(\phi - \phi_{HDk}))2\pi t))] \quad (5)$$

Modification of the Burgess and O'Keefe model

For the simulations presented here, we found it necessary to make one modification to the initial Burgess and O'Keefe model (*12*). In equation 4, the effect of speed s and head direction ϕ on dendritic subthreshold oscillation frequency was altered to be proportional to the baseline frequency of subthreshold oscillations f. Thus, equation 4 was modified to insert f, and change the scaling parameter B to B_H as follows:

$$v_d = \cos((f + fB_H s\cos(\phi - \phi_{HD}))2\pi t) \quad (6)$$

This modification results in a dependence of grid cell field spacing on subthreshold oscillation frequency f, as shown in Fig. 4 and Figs. S4, S5 and S7. The model provides a direct functional link between the frequency of single cell subthreshold oscillations (f) recorded intracellularly in vitro and the grid cell spacing (G) for neurons in awake, behaving animals. This link requires setting of a single parameter B_H based on a scaling factor H determined directly from our experimental results and those from the Moser laboratory (*9-11*).

Mathematical analysis and setting of the parameter B_H

The following mathematical analysis shows how the scaling factor H can be incorporated into the model to allow the model to generate correct grid cell spacing (G) based on subthreshold oscillation frequency (f). Mathematical analysis of the model shows how to set the parameter B_H, by deriving the dependence of the parameter B_H on the scaling factor H from the data.

First we must analyze how parameters in the Burgess model will influence grid cell spacing G. In the Burgess model, the distance between grid fields is determined by the interaction of individual dendrites with the soma, so we will first consider the periodicity of the interference pattern of a single individual oscillating dendrite with the soma.

Consider the periodicity of this interaction as a rat moves at a constant speed s in the optimal tuning direction of one head direction cell, such that $\phi_{rat}=\phi_{HD}$. In this case, the dendritic frequency f_d takes the value: $f + fBs$. This frequency interacts with the soma frequency f. The sum of two interacting sinusoidal waves with frequencies f_1 and f_2 shows an interference pattern with an overall envelope with a frequency equal to the difference in frequencies f_1-f_2. In acoustics, this is called the "beat" frequency, and is here labelled f_b. The difference in dendritic frequency $f+fB_Hs$ and soma frequency f is just fB_Hs.

This beat frequency $f_b=fB_Hs$ can be used to calculate the time period of an individual cycle, or T_b. For temporal oscillations, $T_b=1/f_b$. This time period can be quite large for frequencies that are close to each other. This beat frequency can be considered a measure of the time between cycles of spiking activity of the cell. Consider a rat starting in the center of a grid field, where the dendrite and soma are firing at the same phase, and the summed depolarization is sufficient to cause spiking activity. As the rat moves, the speed causes a shift in dendritic frequency, and the difference in frequency between the dendrite and the soma causes a progressive phase difference reducing constructive interference and increasing destructive interference, which results in less depolarization on each cycle of oscillation and a cessation of firing. If we assume the rat is moving with constant speed s, then we can compute the distance the rat travels in the preferred direction of the head direction cell before the cell starts to fire again (when the frequencies start to show constructive interference and contribute to depolarizing the cell enough to bring it to firing threshold). This distance λ_b is simply the period of the interference cycle T_b times the speed s. Thus, $\lambda_b = sT_b$.

The distance covered between periods of constructive interference for an individual dendrite is not quite the grid cell spacing, because in the model the hexagonal pattern of grid fields results from multiple interacting dendrites. The distance traversed during the period T_b corresponds to the height of an equilateral triangle (60 degree angles), whereas the grid cell spacing G corresponds to the length of one side of the equilateral triangle. Thus, if we consider half of the equilateral triangle, we have a right triangle with one

side λ_b, one side $G/2$, and the hypotenuse of length G. The trigonometric relationship $G^2=(G/2)^2+\lambda^2$ yields $G = \lambda_b(2/\sqrt{3})$. This has been used in models of grid cell effects (*19*).

We can now substitute for λ_b and obtain the equation: $G = (s/f_b)(2/\sqrt{3})$. Then, we can substitute for f_b and obtain: $G = (s/sfB_H)(2/\sqrt{3})$. Note that the speed value s cancels out in this equation, so that speed does not influence grid spacing G, and we obtain: $G = (1/fB_H)(2/\sqrt{3})$. The cancelling of speed is an important feature of the model for giving constant grid spacing G regardless of the movement speed of the rat, as shown in the simulations by Burgess (*12,13*) and our own simulations using both random trajectories and real data from the Moser laboratory (*10*).

Using the equation: $G = (1/fB_H)(2/\sqrt{3})$, we rearrange G and B_H to show the dependence of B_H on the experimental values, obtaining:

(7) $$B_H = (1/fG)(2/\sqrt{3})$$

This equation clearly shows that computation of the value of B_H necessary for the simulation requires computation of the value of fG derived from the experimental data. Therefore, we can insert our experimentally derived relationship $H=fG$ into the equation, obtaining:

(8) $$B_H = 2/(\sqrt{3}H)$$

Substituting H = 300 Hz-cm in the equation yields the value for the parameter B_H = 0.00385. The units of B_H are the reciprocal of the units of H, which can be re-arranged to give the reciprocal of speed times the scaling of grid units to subthreshold oscillation cycles (sec/cm)(grid units/cycles(mpo)). The value of B_H derived directly from the experimentally determined scaling constant (H) was used in the simulations to test the simulated grid spacing (G) obtained for subthreshold oscillation frequencies (f) at different positions (z) along the dorsal to ventral axis. As shown in Fig. 4 and in Fig. S4 and Fig. S7, setting this single parameter in the model results in a remarkably consistent relationship between simulated data and real data values for the subthreshold oscillation frequencies (f) tested in the model and the grid cell spacing (G) generated by the model across the full range of values for both variables at different anatomical positions z along the dorsal to ventral extent of the entorhinal cortex.

Simulations of subthreshold oscillation frequency and grid spacing

The Burgess and O'Keefe model was used with the experimentally derived scaling factor H to simulate grid cell properties of entorhinal cortex neurons. The pattern of interference between subthreshold oscillations due to input from head direction cells causes the characteristic properties of grid cell firing (Fig. 4). Altering the baseline membrane oscillation frequency f to high frequencies to represent the properties of dorsal neurons found here causes grid cell firing with small distances between fields matching the experimental data. Altering the baseline frequency f to low frequencies to represent properties of ventral neurons found here causes a grid cell firing pattern with larger

distances between fields, again matching experimental data (*11*). As quantified in Fig. S7, the model correctly matches experimental data on values of *G* at different anatomical positions *z*, when the baseline frequency *f* is set to the corresponding value of oscillation frequency at anatomical location *z*.

Simulations were run using MATLAB, with firing threshold set at 1.8. The script used for simulations is available by e-mail request to Michael Hasselmo at hasselmo@bu.edu. This script used the modified Burgess and O'Keefe model described above coupled with two methods of guiding the movement of the simulated rat. The rat movements can be generated by an algorithm using random movements with momentum, or they can be guided by the trajectory provided in experimental data by Hafting and Fyhn (*10*) available by download from the Moser laboratory at http://www.cbm.ntnu.no. Simulation data is plotted in the same manner as the plots of experimental data by Hafting, Fyhn and Sargolini (*9-11*), using plots of spike firing in red relative to the rat trajectory in gray, and also plotting the occupancy normalized Gaussian smoothed density of spiking across the environment with maximal rate plotted in red and firing rate of zero plotted in blue.

The grid cell simulations effectively demonstrate the pattern of grid cell firing and the dependence of grid field spacing on membrane potential oscillation frequency with both the experimental trajectory, used for simulations in Fig. 4, and with the random trajectory, used for simulations with a range of different oscillation frequencies shown in Fig. S4A. Our plots of the simulation data used the presentation format used in experimental work. For comparison with the real data, the same types of plots are presented in Fig. S4B for the experimental data on the Moser laboratory web site (*10*). As noted in Equation 6 above, the Burgess model was altered in one way by including dependence of the change in dendrite oscillation on magnitude of subthreshold oscillations. For example, for movement in the preferred direction of that dendrite, this means that the change *fBs* is proportional to the baseline frequency. For a speed of 25 cm/sec, a baseline frequency of 6 Hz will be pushed up to 6.58 Hz, whereas for a baseline frequency of 3 Hz, it will be increased to 3.29 Hz. The fact that the shift is proportional to baseline frequency may be consistent with the larger increase in frequency at -45 mV relative to -50 mV seen for higher frequencies in dorsal neurons in Fig. 1C.

The simulation is completely robust to high variation in movement direction and speed, consistently showing localized patterns of grid field firing. To make this clearer, Fig. S5 shows the pattern of grid cell firing with red dots on the trajectory after different periods of exploration. Similar to previously published data in Fig. 6A of (*10*), the simulation shows clear grid cell firing fields even for the initial 40 seconds of running trajectory (2000 steps), which fits with the grid pattern seen over the subsequent 7 minutes (24000 steps).

In this model, the interference between subthreshold oscillations provides a continuous update of spatial location based on continuous heading direction and speed. However, the same property of quantal interference patterns from continuous changes in subthreshold frequency may be a general neural mechanism for coding and updating

other continuous dimensions, including time. This could allow coding of associations between particular time intervals and sensory input, possibly from lateral entorhinal cortex (*20*), which could be utilized in encoding of sequences for episodic memory (*21*). This work suggests that important properties of neural processing may arise from synaptic inputs regulating interference between intrinsic oscillatory mechanisms in different parts of a neuron.

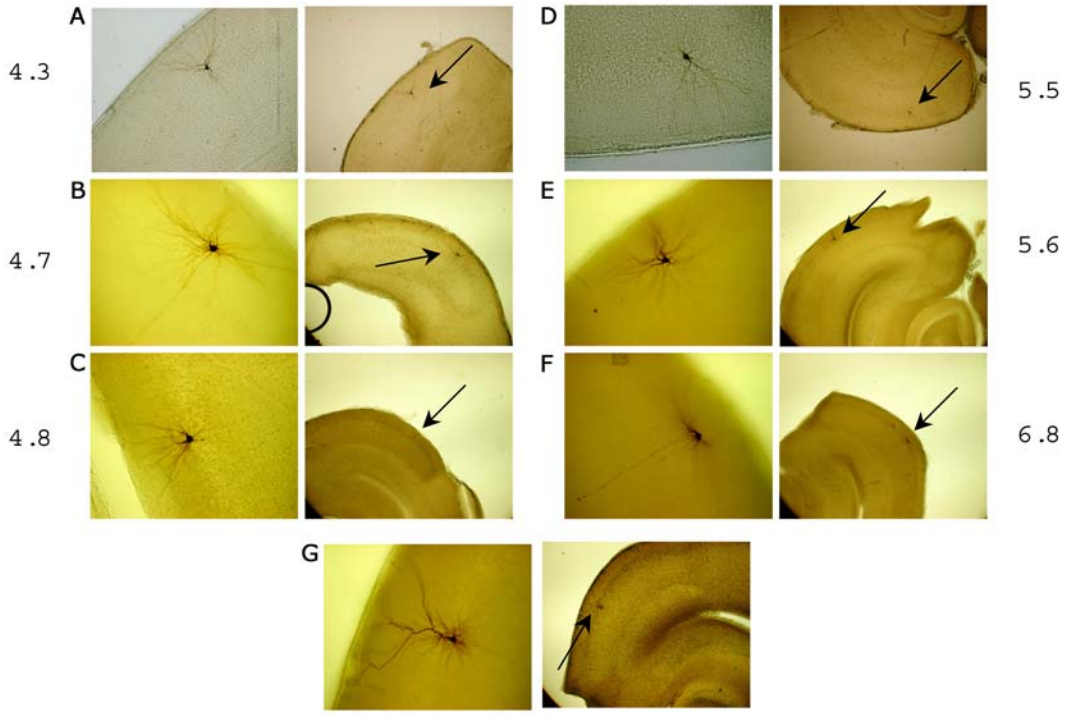

Fig. S1: Examples of biocytin staining of individual neurons tested for this study in layer II of medial entorhinal cortex. **A-F:** Examples of cells with stellate morphology from different distances (mm) along the dorsal to ventral axis (numbers provided are mm from dorsal surface). For each cell, the right side shows the location of the cell in layer II of medial entorhinal cortex indicated by the black arrow. On the left side the cell morphology is shown at higher magnification. **G:** Example of a cell with a non-stellate, pyramidal-like morphology.

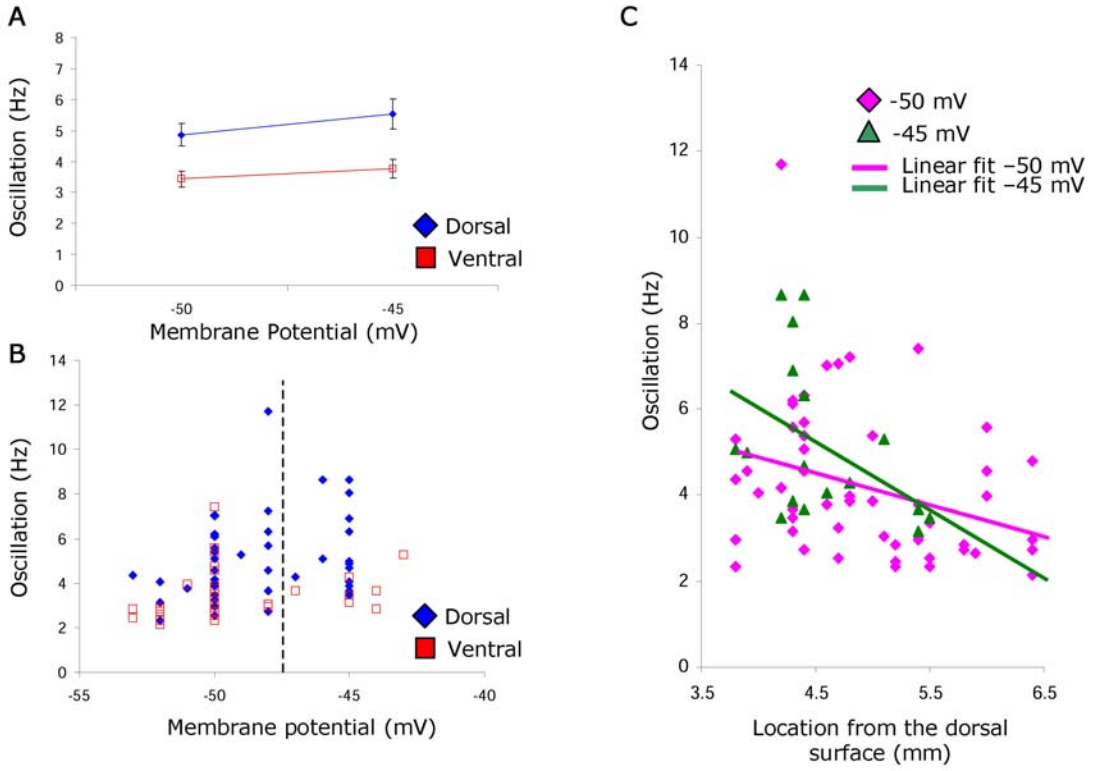

Fig. S2: Neurons show higher frequency of subthreshold oscillations in dorsal entorhinal cortex and lower frequency of subthreshold oscillations in ventral entorhinal cortex, as computed from the power spectra of neuronal responses. **A.** Mean frequency of subthreshold oscillations for dorsal (3.8 − 4.9 mm Bregma) and ventral (4.9 − 7.1 mm Bregma) as determined by the power spectra analysis at approximately −50 mV and −45 mV. **B**. Frequency of subthreshold oscillations from dorsal and ventral portions of medial entorhinal cortex compared to the average membrane potential during subthreshold oscillations. **C.** Scatter plot of the subthreshold oscillation frequency of neurons (determined by power spectra) plotted in relation to the distance of the slice from the dorsal surface of the brain. Note the decrease in frequency from dorsal to ventral entorhinal cortex. Although the mean oscillation measurement with the power spectra was lower compared to the mean oscillation measurement with the autocorrelation for both dorsal and ventral cells, the dorsal cells were proportionally faster than the ventral cells in a similar manner for both sets of data (Autocorrelation at −50 mV = 1.53 times faster; Power spectra at −50 mV = 1.43 times faster; Autocorrelation at −45 mV = 1.47 times faster; Power spectra at −45 mV = 1.47 times faster.

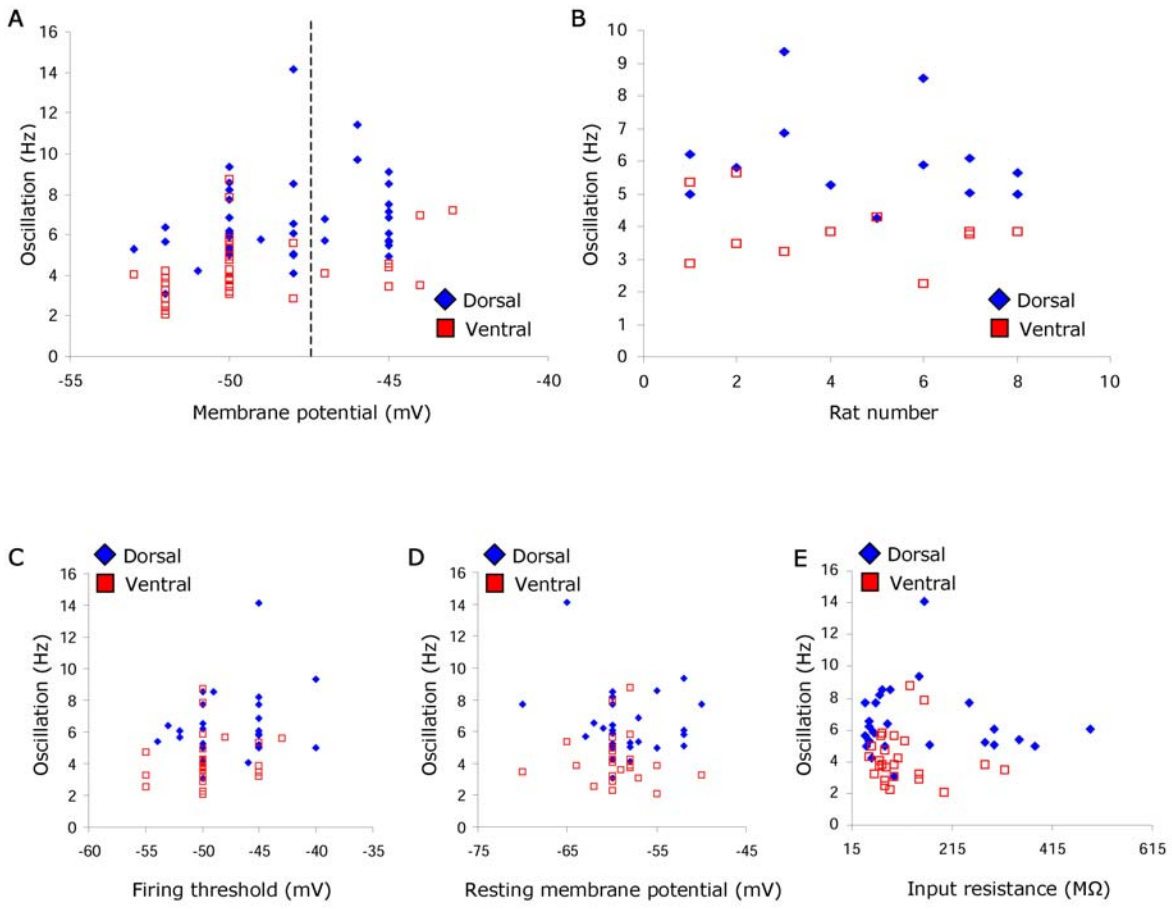

Fig. S3: **A.** Frequency of subthreshold oscillations, as determined by the autocorrelation analysis, plotted relative to the average membrane potential during the oscillation. More depolarized membrane potentials show high oscillation frequency. **B.** Comparison of oscillation frequency from dorsal and ventral slices taken from individual rats with rat number plotted on the x axis and frequency on the y axis. Notice that the ventral versus dorsal difference appeared consistently within separate individual rats on different days. **C.** Frequency of subthreshold oscillation at −50 mV, as determined by the autocorrelation analysis, compared to firing threshold of the cell. There is no systematic relationship between frequency of subthreshold oscillations and firing threshold. **D**. Frequency of subthreshold oscillation at −50 mV, as determined by the autocorrelation analysis, compared to the resting potential of the cell. There is no systematic relationship between frequency and resting membrane potential. **E**. Input resistance compared to subthreshold oscillation frequency. There is no systematic change in frequency with input resistance.

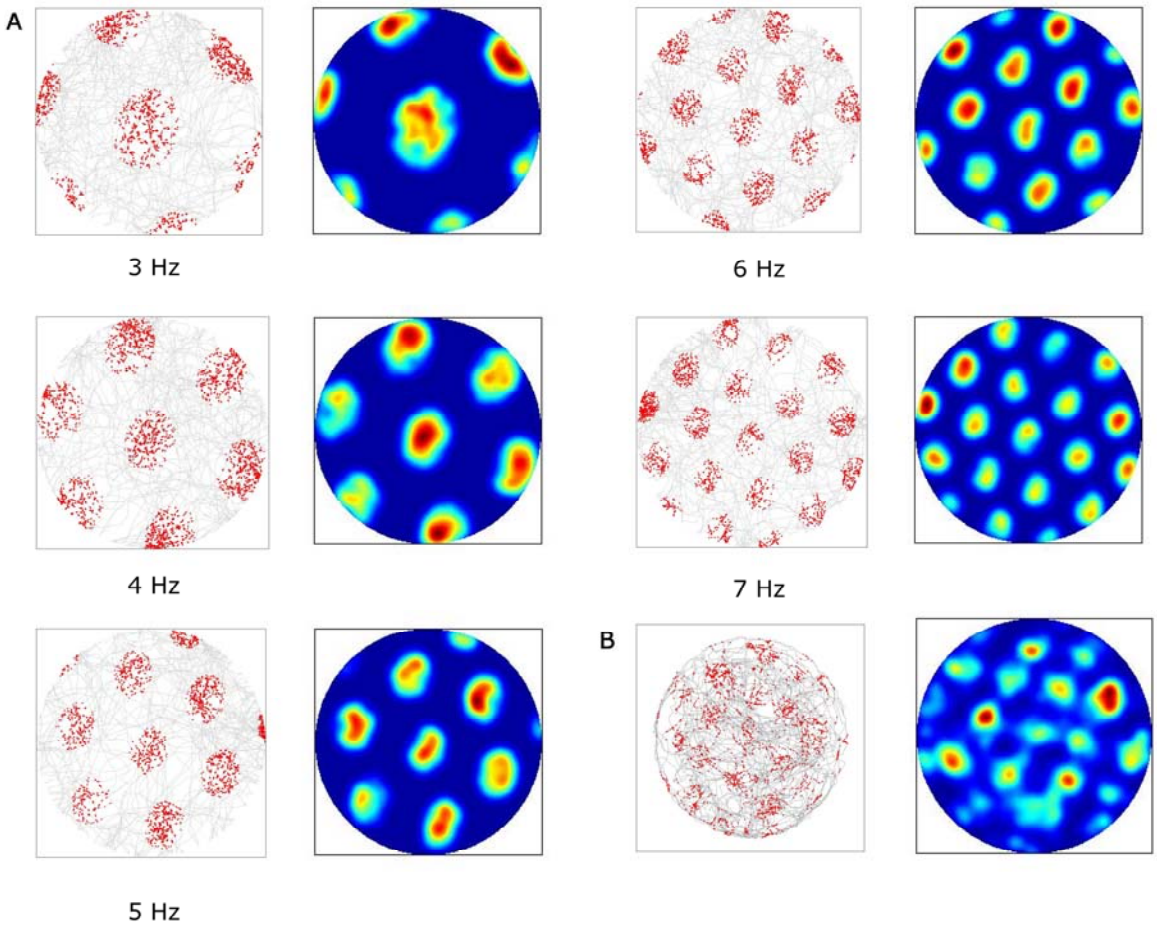

Fig. S4:
A. Simulated pattern of firing for different simulated grid cells with different intrinsic subthreshold oscillation frequencies during random exploration of the circular environment. For each pair of plots, the frequency of subthreshold membrane potential oscillations is marked, ranging from 3 Hz to 7 Hz. For each frequency, the plot on the left shows the random trajectory in gray and the location of simulated rat when spikes were generated in red. The plot on the right shows the Gaussian smoothed, occupancy normalized density of spiking. As can be seen, low frequencies of intrinsic oscillations result in large distances between grid cells (large grid spacing) and fewer grid fields in the environment, while high frequencies of membrane potential oscillations result in smaller distances between grid cells (small grid spacing) and more grid fields in the same area. **B.** Example of grid cell firing properties as described by Hafting and Fyhn in the Moser laboratory (*10*). The distribution of spike location and spike density in the experimental data resembles that seen in the simulation output.

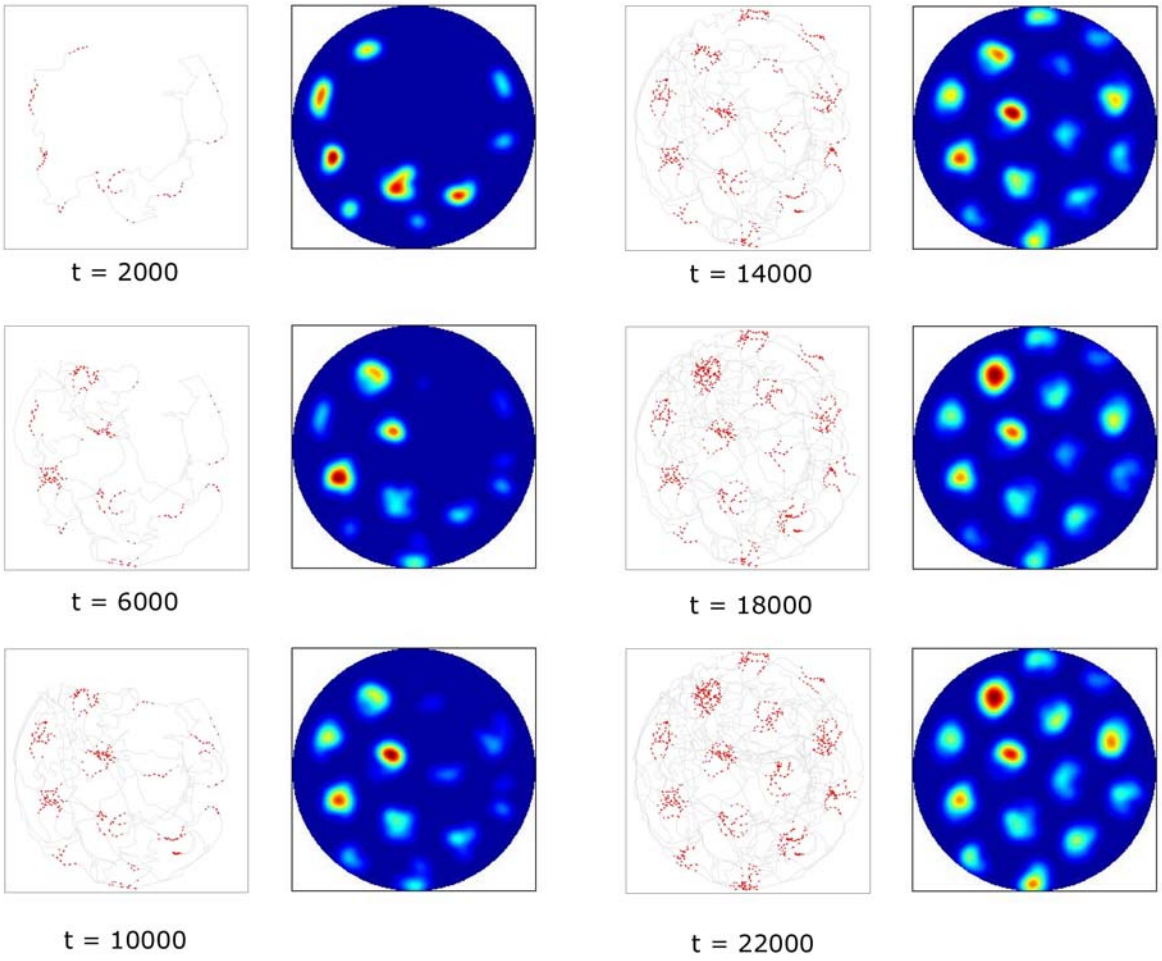

Fig. S5:
Demonstration of the firing activity of a simulated grid cell over time as a simulated rat follows the trajectory obtained from experimental data made available from the Moser laboratory (*10*). Each figure on the left shows the trajectory up to that point in gray, and the individual spikes in red plotted at the location of the virtual rat when threshold was crossed. Activity is shown after a different number of time steps (each step is 20 ms, so that 2000 steps = 40 seconds). Note that the spiking occurs in the correct grid field locations regardless of the trajectory of the rat during the intervening time. During 22000 time steps (440 secs), the spiking activity has appeared in a full grid pattern. The plots on the right show the occupancy normalized Gaussian smoothed average of spiking density at each time point.

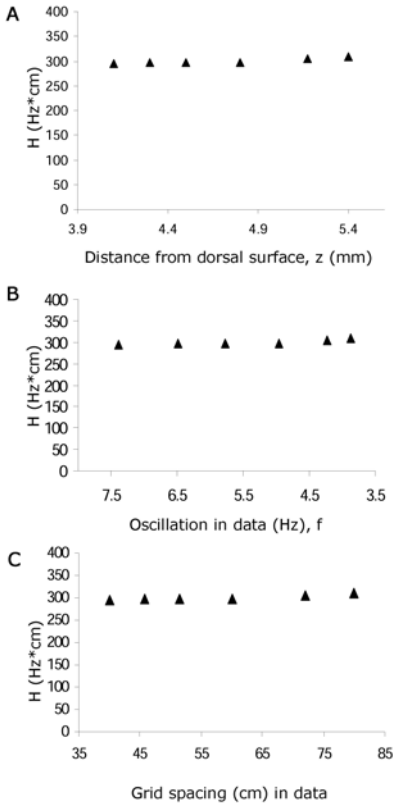

Fig. S6:
Value of the experimentally derived scaling factor (*H*) based on experimental data. The value of $fG = H$ (Hz-cm) at different anatomical positions *z* was determined by multiplication of the experimentally determined values from our data on subthreshold oscillation frequency *f* (in Hz) and the data on grid cell spacing *G* (in cm) estimated from previous work (*11*). The data points *f* and *G* were determined from the value of the linear regression line at anatomical position *z*. The same data on *H* is plotted in relation to the three values *z*, *f* and *G* used to compute each data point. **A.** Plot of the values of *H* (Hz-cm) in relation to the anatomical position *z* from which *f* and *G* were obtained. **B.** Plot of the values of *H* in relation to the frequency *f* (Hz) used for each point. **C.** Plot of the values of *H* in relation to the grid spacing *G* (cm) used for each point.

Values of the data estimated from regression lines were as follows:

Position *z* (mm)	4.1	4.3	4.5	4.8	5.2	5.4
Frequency *f* (Hz)	7.38	6.48	5.77	4.96	4.23	3.87
Grid spacing *G* (cm)	40.1	46.1	52.1	61.1	72.2	79.1
H (Hz*cm)	296	299	301	303	305	306

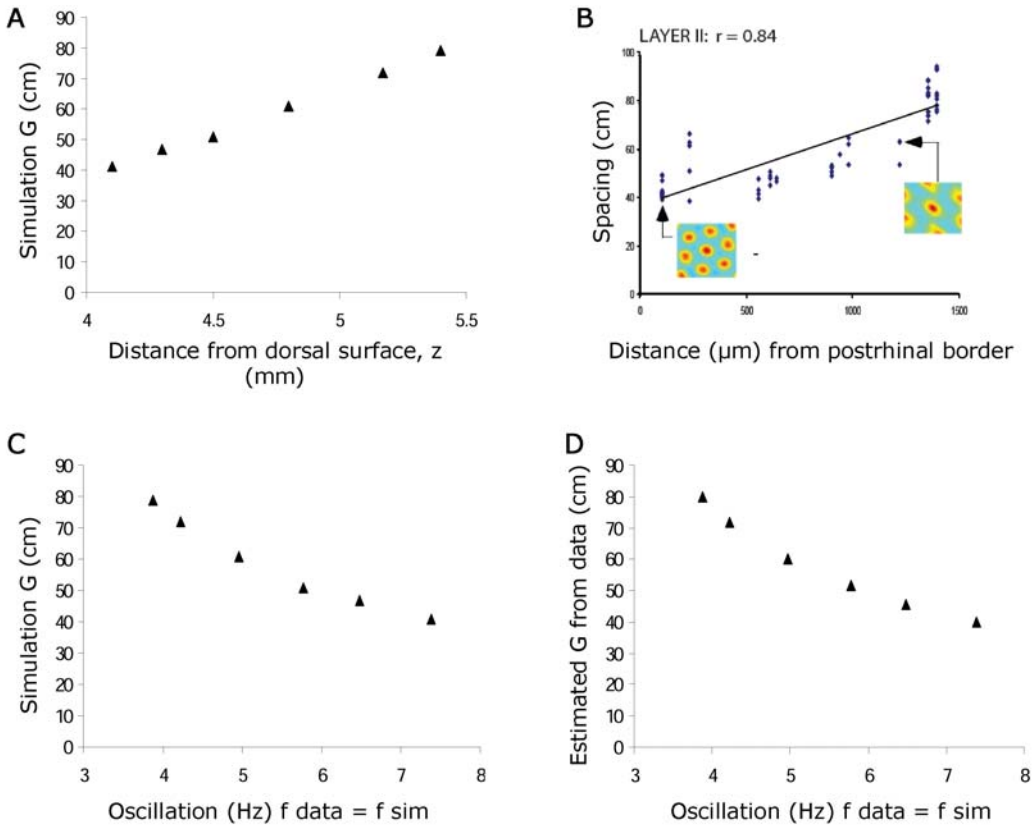

Fig. S7:
The simulation of the Burgess model shows correct scaling of subthreshold oscillation frequency to grid field spacing, due to use of the experimentally determined value of $B_H = 2/(\sqrt{3}H)$. For the oscillation frequency (*f*) at a particular position *z*, the model correctly replicates the grid cell spacing found with in vivo recording at that particular position z (*11*). **A.** Plot of grid spacing *G* (cm) produced by simulations. *G* is plotted relative to the anatomical position z (in mm from dorsal surface) of the data used for setting the frequency *f* in the model. **B.** Reproduction of the figure showing plot of experimentally determined grid spacing *G* estimated from the data versus anatomical position *z* of recorded cells (*11*). Note that the experimental data plot uses z in microns (not mm) starting from the border of postrhinal cortex. **C.** Grid spacing *G* (cm) produced by each simulation plotted relative to the frequency (*f*) used for each simulation. **D.** Estimated grid cell spacing *G* from experimental data at specific anatomical positions (*11*) plotted relative to the estimated membrane potential oscillation frequency (*f*) obtained at the corresponding anatomical position in the slice data presented here.

Supplemental References

1. C. Dickson, A. Alonso, *J. Neurosci* **17**, 6729-6744 (1997).
2. C. T. Dickson *et al.*, *J Neurophysiol* **83**, 2562-79 (2000).
3. G. Paxinos, C. Watson, *The rat brain in stereotaxic coordinates* (Academic Press, San Diego, CA, 1998).
4. B. N. Hamam, D. G. Amaral, A. Alonso, *J Comp Neurol* **451**, 45-61 (2002).
5. B. Tahvildari, A. Alonso, *J Comp Neurol* **491**, 123-40 (2005).
6. R. Klink, A. Alonso, *Hippocampus* **7**, 571-583 (1997).
7. A. Alonso, R. Klink, *J. Neurophysiol.* **70**, 128-143 (1993).
8. E. Fransen, A. A. Alonso, C. T. Dickson, J. Magistretti, M. E. Hasselmo, *Hippocampus* **14**, 368-84 (2004).
9. M. Fyhn, S. Molden, M. P. Witter, E. I. Moser, M. B. Moser, *Science* **305**, 1258-64 (2004).
10. T. Hafting, M. Fyhn, S. Molden, M. B. Moser, E. I. Moser, *Nature* **436**, 801-6 (2005).
11. F. Sargolini *et al.*, *Science* **312**, 758-62 (2006).
12. N. Burgess, C. Barry, K. J. Jeffery, J. O'Keefe, paper presented at the Computational Cognitive Neuroscience Meeting, Washington, D.C. (Nov. 11, 2005).
13. N. Burgess, C. Barry, J. O'Keefe, *Hippocampus*, in press.
14. J. O'Keefe, N. Burgess, *Hippocampus* **15**, 853-66 (2005).
15. J. O'Keefe, M. L. Recce, *Hippocampus* **3**, 317-330 (1993).
16. M. Lengyel, Z. Szatmary, P. Erdi, *Hippocampus* **13**, 700-14 (2003).
17. A. Kamondi, L. Acsady, X. J. Wang, G. Buzsaki, *Hippocampus* **8**, 244-261 (1998)
18. H. T. Blair, A. C. Welday, K. Zhang, *J. Neurosci.* in press.
19. T. Solstad, E. I. Moser, G. T. Einevoll, *Hippocampus* 16:1026-31 (2006).
20. E.L. Hargreaves, G. Rao, I. Lee, J.J. Knierim, *Science* 308: 1792-4 (2005).
21. M. E. Hasselmo, H. Eichenbaum, *Neural Netw* **18**, 1172-90 (2005).